

Research Article

New Method for Analyzing the Flutter Stability of Hingeless Blades with Advanced Geometric Configurations in Hovering

Si-wen Wang ¹, Jing-long Han ¹, Quan-long Chen,² Hai-wei Yun,¹ and Xiao-mao Chen¹

¹State Key Laboratory of Mechanics and Control of Mechanical Structures, Nanjing University of Aeronautics and Astronautics, Nanjing 210016, China

²Chongqing Enstrom General Aviation Institute of Technology, Chongqing 401135, China

Correspondence should be addressed to Si-wen Wang; nmghappy@126.com

Received 6 October 2019; Accepted 20 December 2019; Published 17 February 2020

Academic Editor: Joseph Morlier

Copyright © 2020 Si-wen Wang et al. This is an open access article distributed under the Creative Commons Attribution License, which permits unrestricted use, distribution, and reproduction in any medium, provided the original work is properly cited.

A new method used to analyze the aeroelastic stability of a helicopter hingeless blade in hovering has been developed, which is especially suitable for a blade with advanced geometric configuration. This method uses a modified doublet-lattice method (MDLM) and a 3-D finite element (FE) model for building the aeroelastic equation of a blade in hovering. Thereafter, the flutter solution of the equation is calculated by the V-g method, assuming blade motions to be small perturbations about the steady equilibrium deflection. The MDLM, which is suitable to calculate the unsteady aerodynamic force of nonplanar rotor blade in hovering, is developed from the doublet-lattice method (DLM). The structural analysis tool is the commercial software ANSYS. The comparisons of the obtained results against those in the literatures show the capabilities of the MDLM and the method of structural analysis. The flutter stabilities of swept tip blades with different aspect ratios are analyzed using the new method developed in this work and the usual method on the basis of the unsteady strip theory and beam model. It shows that considerable differences appear in the flutter rotational velocities with the decrease of the aspect ratio. The flutter rotational velocities obtained by the present method are evidently lower than those obtained by the usual method.

1. Introduction

Hovering is the most important flight state of a helicopter. The flutter stability of hovering is directly related to flight safety. Numerous methods on stability characteristics of hingeless rotors in hovering have been developed to obtain an accurate flutter stability boundary. The aeroelastic equations of their methods are usually obtained by aerodynamic models, which are formed by quasisteady [1] or unsteady strip theories [2], and the structural dynamic models, which are formed by moderate [3] and large deflection beam [4] theories or other refined beam theories [5–7], considering the geometrical nonlinearity. Generally, for the flutter solution of the aeroelastic equations, the nonlinear steady state is obtained first and then the flutter solution, assum-

ing that the flutter motion is a small perturbation about the equilibrium position [1–8]. The blades of aforementioned researches are made of isotropic [3] or composite [8] material with high aspect ratios and simple planform shapes. With the development of computational fluid dynamics (CFD), the method of rotorcraft aeroelastic tight coupling of computational structural dynamics (CSD) and CFD has been used for rotor blade aeroelastic stability analysis recently [9, 10]. Although the CFD/CSD coupled method can get better predictions of rotor stability, the computational cost of this method is very high [11], and CSD models are mostly built with beams mentioned above.

The majority of manufacturers choose blades with advanced geometric configurations, such as the ERATO [12] blade with reduced Blade Vortex Interaction (BVI) noise

signature to increase the flight speed and have good aeroacoustic behavior. The advanced blade with a complicated tip and a small aspect ratio deviates largely from the classical rectangular one. The modal analysis using the beam model of blades may be unsuitable due to the deviation of a planform shape. Truong [13] studied the dynamic characteristics of the ERATO using 3-D finite element and 1-D beam analyses in MSC software. Natural frequencies are calculated at various rotor rotational speeds. The predictions of the 3-D finite element model that correlate with the experimental results are more precise than those of the (1-D+2-D) model, within a 5% relative error. Yeo [14] et al. are motivated by the above research to study the difference between 1-D beam and 3-D finite element analyses for advanced geometry blades, which have tip sweep, tip taper, and planform variations near the root and physics behind them. Differences occur when coupling generated from geometry (tip sweep) or material (composite) emerges, especially for high-frequency modes. Thereafter, Kee and Shin [15] use an eighteen-node solid-shell finite element to model the blade structures and give the differences of natural frequencies between the one-dimensional beam and three-dimensional solid models. As the blade aspect ratio decreases, considerable differences appear in the bending and torsion modes. Evidently, the accuracy of modal calculation directly determines the reliability of flutter analysis. Here comes the conclusion that the commonly used aeroelastic model constructed by strip theory and the 1-D beam model is unsuitable for the flutter stability analysis of blades with advanced geometric configurations in hovering. It is also easy to conclude that the CFD/CSD tight coupling approach using 3-D solid structure models instead of beam models will increase computing costs inevitably when there is already a large amount of computation. A new high-efficiency approach of advanced blade flutter analysis is sorely necessary. So far, no relevant literature has been reported on that.

A new method of rotor flutter analysis, using a 3-D finite element model and a modified doublet-lattice method (MDLM) to establish the aeroelastic equation, is developed to solve the abovementioned problems. ANSYS is applied to the numerical analysis of blade structure, and the blades are discretized by the 3-D solid element. In aerodynamic calculation, compared with the aerodynamic models mentioned above, one of the major advantages of the DLM [16] is that motions of parts of the wing section can be considered, which makes the DLM more suitable for being coupled with the 3-D finite element model to establish the aeroelastic model than the strip theory. The other one is that the DLM is much more effective than the CFD method. However, the DLM cannot be used for rotor flutter analysis directly because the inflows change over the location of the blade and the pretwist cannot be ignored. The MDLM, which overcomes the above difficulties to calculate the unsteady aerodynamic of rotor blades in hovering, is developed from the DLM. The method of solving the aeroelastic equations is basically the same as the abovementioned

one. The nonlinear steady state is obtained first to linearize the flutter equations, based on the small perturbation assumption. Thereafter, the linearized flutter equations are solved through the V-g method [2]. The structural analysis method and MDLM of rotor blades are verified by literature examples. Thereafter, the new and usual methods of rotor flutter analysis are used for solving the flutter rotational velocities of advanced blades in hovering, which have different ratio aspects. The comparison of these two methods is conducted systematically to understand the differences.

2. Analysis

2.1. Modified Doublet Lattice Method (MDLM)

2.1.1. Correction of the Nonplanar Hypothesis. The DLM assumes the lifting surfaces as a planar plate without pretwist angles; that is, in the aerodynamic coordinate frame of the sending panel, the chordwise component of the normal vector of the receiving panel is equal to zero [17]. Pretwist angles are widely used in helicopter rotor blades, which have a great influence on aerodynamic forces. Hence, the DLM's assumption is unsuitable for rotor blades. On the basis of the DLM, the MDLM is developed for calculating unsteady aerodynamic loads on nonplanar lifting surfaces in subsonic flows.

Normal wash velocity [18] of receiving point (x, y, z) induced by the surface motion can be written as follows:

$$\bar{w} = \frac{1}{8\pi} \int_A \frac{U_\infty \Delta \bar{p} K(\bar{x}, \bar{y}, \bar{z}, \omega, M_\infty)}{q_d} dA \quad (1)$$

where $\bar{x} = x - \hat{\xi}$, $\bar{y} = y - \hat{\zeta}$, $\bar{z} = z - \hat{\eta}$, $\Delta \bar{p}$, q_d , U_∞ , and M_∞ are the pressure loading, velocity pressure number, free-flow velocity, and Mach number at sending point $(\hat{\xi}, \hat{\zeta}, \hat{\eta})$, respectively. ω is the circular frequency of vibration of the blade. The kernel function [18] can be expressed as follows:

$$K(\bar{x}, \bar{y}, \bar{z}, \omega, M_\infty) = \lim_{n_c \rightarrow 0} \frac{\partial}{\partial n_c} \left\{ e^{-(i\omega \bar{x}/V)} \int_{-\infty}^{\bar{x}} \frac{\partial}{\partial n_d} \left[\frac{1}{R} e^{(i\omega(\lambda - M_\infty R))/M_\infty} \right] d\lambda \right\}, \quad (2)$$

where

$$\begin{cases} \lambda = x - \hat{\xi}, r = \sqrt{\bar{y}^2 + \bar{z}^2}, R = \sqrt{\lambda^2 + \beta^2 r^2}, \\ \beta^2 = 1 - M_\infty^2, \frac{\bar{\omega} = \omega}{a_\infty \beta^2}, i = \sqrt{-1}. \end{cases} \quad (3)$$

Partial differentiations $\partial/\partial n_c$ and $\partial/\partial n_d$ are taking the derivative of the receiving point and the sending point. ∂

$\partial/\partial n_c$ and $\partial/\partial n_d$ can be expressed by the following formulations:

$$\begin{cases} \frac{\partial}{\partial n_c} = \cos(n_c, x) \frac{\partial}{\partial x} + \cos(n_c, y) \frac{\partial}{\partial y} + \cos(n_c, z) \frac{\partial}{\partial z}, \\ \frac{\partial}{\partial n_d} = \cos(n_d, \hat{\xi}) \frac{\partial}{\partial \hat{\xi}} + \cos(n_d, \hat{\zeta}) \frac{\partial}{\partial \hat{\zeta}} + \cos(n_d, \hat{\eta}) \frac{\partial}{\partial \hat{\eta}}. \end{cases} \quad (4)$$

In the case of small perturbations, the following relations are obtained:

$$\cos(n_d, \hat{\xi}) \ll \cos(n_d, \hat{\zeta}), \cos(n_d, \hat{\eta}). \quad (5)$$

$\cos(n_c, x)$ cannot be ignored due to blade elastic torsion and pretwist. Formulation (4) can be rewritten as follows:

$$\begin{cases} \frac{\partial}{\partial n_c} = \cos(n_c, x) \frac{\partial}{\partial x} + \frac{\partial}{\partial n_{c0}}, \\ \frac{\partial}{\partial n_d} = \cos(n_d, \hat{\zeta}) \frac{\partial}{\partial \hat{\zeta}} + \cos(n_d, \hat{\eta}) \frac{\partial}{\partial \hat{\eta}}, \\ \frac{\partial}{\partial n_{c0}} = \cos(n_c, y) \frac{\partial}{\partial y} + \cos(n_c, z) \frac{\partial}{\partial z}. \end{cases} \quad (6)$$

The kernel function K can be also written as follows:

$$\begin{aligned} K(\bar{x}, \bar{y}, \bar{z}, \omega, M_\infty) = \cos(n_c, x) & \left(\frac{-i\omega}{V} e^{-i\omega\bar{x}/V} \frac{\partial}{\partial n_d} \bar{I} + e^{-i\omega\bar{x}/V} \frac{\partial}{\partial x} \frac{\partial}{\partial n_d} \bar{I} \right) \\ & + e^{-i\omega\bar{x}/V} \lim_{n_c \rightarrow 0} \frac{\partial}{\partial n_{c0}} \frac{\partial}{\partial n_d} \bar{I}, \end{aligned} \quad (7)$$

where

$$\bar{I} = \int_{-\infty}^{\bar{x}} \left[\frac{1}{R} e^{i\bar{\omega}(\lambda - M_\infty R)/M_\infty} \right] d\lambda. \quad (8)$$

Because

$$\begin{cases} \frac{\partial}{\partial \hat{\zeta}} \left[\frac{1}{R} e^{(i\bar{\omega}(\lambda - M_\infty R))/M_\infty} \right] = -\frac{\partial}{\partial y} \left[\frac{1}{R} e^{(i\bar{\omega}(\lambda - M_\infty R))/M_\infty} \right], \\ \frac{\partial}{\partial \hat{\eta}} \left[\frac{1}{R} e^{(i\bar{\omega}(\lambda - M_\infty R))/M_\infty} \right] = -\frac{\partial}{\partial z} \left[\frac{1}{R} e^{(i\bar{\omega}(\lambda - M_\infty R))/M_\infty} \right], \end{cases} \quad (9)$$

and using ψ_s for representing the anhdral of the receiving point and ψ_d for representing the anhdral of the sending point, we can write certain equations as follows:

$$\begin{cases} \cos(n_c, y) = -\sin \psi_s, \cos(n_c, z) = \cos \psi_s, \\ \cos(n_d, \hat{\zeta}) = -\sin \psi_\sigma, \cos(n_d, \hat{\eta}) = \cos \psi_\sigma. \end{cases} \quad (10)$$

And then

$$\begin{cases} \frac{\partial}{\partial n_{c0}} \frac{\partial}{\partial n_d} = - \left[\sin \psi_s \sin \psi_\sigma \frac{\partial^2}{\partial y^2} + \cos \psi_s \cos \psi_\sigma \frac{\partial^2}{\partial z^2} - (\sin \psi_s \cos \psi_\sigma + \cos \psi_s \sin \psi_\sigma) \frac{\partial^2}{\partial y \partial z} \right], \\ \frac{\partial}{\partial n_d} = - \left(-\sin \psi_\sigma \frac{\partial}{\partial y} + \cos \psi_\sigma \frac{\partial}{\partial z} \right). \end{cases} \quad (11)$$

According to the following equations:

$$\begin{cases} \frac{\partial \bar{I}}{\partial z} = \frac{\partial \bar{I}}{\partial r} \frac{\partial r}{\partial z} = \frac{\bar{z}}{r} \frac{\partial \bar{I}}{\partial r}, \frac{\partial \bar{I}}{\partial y} = \frac{\partial \bar{I}}{\partial r} \frac{\partial r}{\partial y} = \frac{\bar{y}}{r} \frac{\partial \bar{I}}{\partial r}, \\ \frac{\partial^2 \bar{I}}{\partial z^2} = \frac{1}{r} \frac{\partial \bar{I}}{\partial r} + \frac{\bar{z}^2}{r} \frac{\partial}{\partial r} \left(\frac{1}{r} \frac{\partial \bar{I}}{\partial r} \right), \frac{\partial^2 \bar{I}}{\partial y^2} = \frac{1}{r} \frac{\partial \bar{I}}{\partial r} + \frac{\bar{y}^2}{r} \frac{\partial}{\partial r} \left(\frac{1}{r} \frac{\partial \bar{I}}{\partial r} \right), \\ \frac{\partial^2 \bar{I}}{\partial y z} = \frac{\bar{y} \bar{z}}{r} \frac{\partial}{\partial r} \left(\frac{1}{r} \frac{\partial \bar{I}}{\partial r} \right), \end{cases} \quad (12)$$

and substituting Equations (11) and (12) into Equation (7), the kernel function can be rewritten as follows:

$$\begin{aligned} K(\bar{x}, \bar{y}, \bar{z}, \omega, M_\infty) = \cos \theta & \left(e^{-i\omega\bar{x}/V} (-\sin \psi_\sigma \bar{y} + \cos \psi_\sigma \bar{z}) \right. \\ & \cdot \left(\frac{-i\omega}{V} \frac{K_1}{r^2} + \frac{\partial K_1}{\partial x} \frac{1}{r^2} \right) \\ & \left. + e^{-i\omega\bar{x}/V} \left(\frac{K_1 T_1}{r^2} + \frac{K_2 T_2}{r^4} \right), \right) \end{aligned} \quad (13)$$

where

$$\begin{cases} K_1 = r \frac{\partial I}{\partial r}, K_2 = r^3 \frac{\partial}{\partial r} \left(\frac{1}{r} \frac{\partial I}{\partial r} \right), \\ T_1 = \cos(\psi_s - \psi_\sigma), T_2 = (\bar{z} \cos \psi_s - \bar{y} \sin \psi_s)(\bar{z} \cos \psi_\sigma - \bar{y} \sin \psi_\sigma), \\ I = - \int_{-\infty}^{\bar{x}} \frac{1}{R} e^{(i\bar{\omega}(\lambda - M_\infty R))/M_\infty} d\lambda. \end{cases} \quad (14)$$

The computational procedure of K_1 and K_2 are given by Landahl [18]. $\partial K_1 / \partial x$ of Equation (13) can be calculated by taking the partial derivative of K_1 with respect to x . The results are given as follows:

$$\begin{cases} K_1 = I_1 + \frac{M_\infty r e^{-ik_1 u_1}}{R(1+u_1^2)^{1/2}}, \\ K_2 = -3I_2 - \frac{ik_1 M_\infty^2 r^2 e^{-ik_1 u_1}}{R^2(1+u_1^2)^{1/2}} - \frac{M_\infty r e^{-ik_1 u_1}}{R(1+u_1^2)^{3/2}} \left[(1+u_1^2) \frac{\bar{\beta}^2 r^2}{R^2} + 2 + \frac{M_\infty r u_1}{R} \right], \\ \frac{\partial K_1}{\partial x} = \frac{\partial I_1}{\partial x} - ik_1 \frac{\partial u_1}{\partial x} \frac{M_\infty r e^{-ik_1 u_1}}{R(1+u_1^2)^{1/2}} + \left(-\frac{\partial R}{\partial x} \frac{M_\infty r}{R^2(1+u_1^2)^{1/2}} - \frac{\partial u_1}{\partial x} \frac{M_\infty r u_1}{R(1+u_1^2)^{3/2}} \right) e^{-ik_1 u_1}, \end{cases} \quad (15)$$

where

$$\begin{cases} u_1 = -\frac{\bar{x} - M_\infty R}{\bar{\beta}^2 r}, R = \sqrt{\bar{x}^2 + \bar{\beta}^2 r^2}, \frac{\partial u_1}{\partial x} = -\frac{1}{\bar{\beta}^2 r} + \frac{M_\infty \bar{x}}{\bar{\beta}^2 r R}, \\ I_0 = \sum_{n=1}^{11} a_n \frac{nc_0 - ik_1}{n^2 c_0^2 + k_1^2} e^{-nc_0 u_1}, \frac{\partial I_0}{\partial x} = \sum_{n=1}^{11} -nc_0 a_n \frac{\partial u_1}{\partial x} \frac{nc_0 - ik_1}{n^2 c_0^2 + k_1^2} e^{-nc_0 u_1}, \\ J_0 = \sum_{n=1}^{11} \frac{a_n e^{-nc_0 u_1}}{(n^2 c_0^2 + k_1^2)^2} \{ n^2 c_0^2 - k_1^2 + nc_0 u_1 (n^2 c_0^2 + k_1^2) - ik_1 [2nc_0 + u_1 (n^2 c_0^2 + k_1^2)] \}. \end{cases} \quad (16)$$

The constants a_n and c_0 of Equation (16) are given by Kalman et al. [19].

If $u_1 \geq 0$, then I_1, I_2 , and $\partial I_1 / \partial x$ will be written as follows:

$$\begin{cases} I_1 = \left\{ \left[1 - \frac{u_1}{(1+u_1^2)^{1/2}} - ik_1 I_0 \right] \right\} e^{-ik_1 u_1}, \frac{\partial I_1}{\partial x} = -ik_1 \frac{\partial u_1}{\partial x} I_1 + \left\{ \left[\frac{u_1^2}{(1+u_1^2)^{3/2}} - \frac{1}{(1+u_1^2)^{1/2}} \right] \frac{\partial u_1}{\partial x} - ik_1 \frac{\partial I_0}{\partial x} \right\} e^{-ik_1 u_1}, \\ I_2 = \frac{1}{3} \left\{ (2 + ik_1 u_1) \left[1 - \frac{u_1}{(1+u_1^2)^{1/2}} \right] - \frac{u_1}{(1+u_1^2)^{3/2}} - ik_1 I_0 + k_1^2 J_0 \right\} e^{-ik_1 u_1}, \end{cases} \quad (17)$$

And if $u_1 < 0$, then I_1 , I_2 , and $\partial I_1/\partial x$ can be rewritten as follows:

$$\begin{cases} I_1 = 2 \operatorname{Re} [I_1(0, k_1)] - \operatorname{Re} [I_1(-u_1, k_1)] + i \operatorname{Im} [I_1(-u_1, k_1)], \\ I_2 = 2 \operatorname{Re} [I_2(0, k_1)] - \operatorname{Re} [I_2(-u_1, k_1)] + i \operatorname{Im} [I_2(-u_1, k_1)], \\ \frac{\partial I_1}{\partial x} = 2 \operatorname{Re} \left[\frac{\partial I_1}{\partial x}(0, k_1) \right] - \operatorname{Re} \left[\frac{\partial I_1}{\partial x}(-u_1, k_1) \right] + i \operatorname{Im} \left[\frac{\partial I_1}{\partial x}(-u_1, k_1) \right]. \end{cases} \quad (18)$$

2.1.2. Application of the MDLM on Blade. In the MDLM, the lifting surface of a blade is divided into trapezoidal panels, which have different freestream velocities. The freestream velocity and the reduction frequency are assumed to be constant within the same panel to satisfy the basic assumption and condition of the MDLM based on the DLM. Each panel contains a line of constant strength point doublets along the quarter-chord line and a control point located at the 3/4 chord point at midspan. Substituting the coordination of the control point (x_j, y_j, z_j) and the doublet point (x_j, y_j, z_j) into Equations (1) and (13), the normal wash velocity \bar{w}_{ij} of the control point can be given as follows:

$$\bar{w}_{ij} = \frac{U_j}{8\pi q_{dj}} \Delta \bar{p}_j \iint_{S_j} K_{ij} dS. \quad (19)$$

In Equation (19), U_j is the freestream velocity of the j th panel, S_j is the area of the j th panel, and $\Delta \bar{p}_j$ is the pressure difference per unit area of the j th panel. The dynamic pressure is given by $q_{dj} = 0.5\rho_\infty U_j^2$, where ρ_∞ is the air density. Let the pressure difference on the unit length of 1/4 chord of the j th panel be $\Delta \bar{p}$. To make the distribution of $\Delta \bar{p}$ on 1/4 chord equivalent to that of $\Delta \bar{p}_j$ on the j th panel, their relationship is as follows:

$$\Delta \bar{p}_j l_j = \Delta \bar{p}_j S_j, \quad (20)$$

where l_j is the length of the 1/4 chord of the j th panel. Here, $S_j = (l_j \cos \chi_j) \Delta x_j$, where χ_j is the sweep angle of the doublet line and Δx_j is the average chord. The pressure difference across surface $\Delta \bar{p}_j$ can be written as $\Delta \bar{p}_j = (1/2)\rho_\infty U_j^2 \Delta \bar{c}_{pj}$, where $\Delta \bar{c}_{pj}$ is the coefficient of the pressure difference. Substituting S_j and $\Delta \bar{p}_j$ into Equation (20), $\Delta \bar{p}$ can be rewritten as follows:

$$\Delta \bar{p}_j = \frac{1}{2} \rho_\infty U_j^2 \Delta x_j \cos \chi_j \Delta \bar{c}_{p(j)}. \quad (21)$$

Transform the area integral of Equation (19) into a line integral, and then the normal wash velocity is obtained as follows:

$$\bar{w}_{ij} = \left(\frac{U_j}{8\pi} \Delta x_j \cos \chi_j \int_{l_j} K_{ij} dl \right) \Delta \bar{c}_{p(j)} = D_{ij} \Delta \bar{c}_{p(j)}, \quad (22)$$

where

$$D_{ij} = \frac{U_j}{8\pi} \Delta x_j \cos \chi_j \int_{l_j} K_{ij} dl. \quad (23)$$

The downwash factor D_{ij} can be obtained by the steady downwash factor D_{0ij} and incremental oscillatory downwash factors D_{1ij} and D_{2ij} , where

$$D_{ij} = D_{0ij} + D_{1ij} + D_{2ij}. \quad (24)$$

The steady downwash factor D_{0ij} is derived from horseshoe vortex considerations. The difference from the traditional method given by Hedman [20] is that the infinite free vortex is replaced by the wake shed from the blade. The induced velocities of the wake on the panels are calculated by the classical blade element momentum theory and considered to be steady and uniform along the blade length [21]. For brevity, the derivation processes of incremental oscillatory downwash factors D_{1ij} and D_{2ij} are not presented, which can be referred to the literature [20]. The numerical form of Equation (1) in matrix notation becomes

$$[w] = [D][\Delta c_p], \quad (25)$$

The differential pressure coefficient vector $[\Delta c_p]$ can be obtained by $[\Delta c_p] = [D]^{-1}[w]$. For the j th panel, the pressure difference located at the 1/4 chord point at the midspan of the panel can be obtained by $F_{aj} = q_{dj} \Delta S_j \Delta c_{pj}$. Thereafter, the aerodynamic load vector is obtained in the form of a matrix by the following:

$$[F_a] = [q_d][\Delta S][D]^{-1}[w], \quad (26)$$

where

$$[q_d] = \begin{pmatrix} q_{d1} & \cdots & 0 \\ \vdots & \ddots & \vdots \\ 0 & \cdots & q_{dn} \end{pmatrix}, \quad (27)$$

$$[\Delta S] = \begin{pmatrix} \Delta S_1 & \cdots & 0 \\ \vdots & \ddots & \vdots \\ 0 & \cdots & \Delta S_n \end{pmatrix}.$$

2.2. Structure Modeling. Considering the geometric nonlinearity, the nonlinear forced undamped vibration equation of the blade can be simply obtained by

$$\mathbf{M}^{ss}(\Omega, q_s)[\ddot{q}_s] + \mathbf{K}^{ss}(\Omega, q_s)[q_s] = [F_s], \quad (28)$$

where $[q_s]$ is the displacement vector and $[F_s]$ is the structural load vector. \mathbf{M}^{ss} and \mathbf{K}^{ss} are the structural mass

matrix and stiffness matrix, respectively, and the functions of rotational speed Ω and q_s . Equation (28) is transformed into the modal space by writing

$$[p_s] = \Phi_s^T [q_s], \quad (29)$$

where Φ_s is the modal matrix and $[p_s]$ is the vector of eight generalized coordinates in the modal space. Substituting Equation (29) into Equation (28), the normal equation can be rewritten as follows:

$$\bar{\mathbf{M}}_s(\Omega, p_s)[\ddot{p}_s] + \bar{\mathbf{K}}_s(\Omega, p_s)[p_s] = [\bar{F}_s], \quad (30)$$

where $\bar{\mathbf{M}}_s = \Phi_s^T \mathbf{M}^{ss} \Phi_s$, $\bar{\mathbf{K}}_s = \Phi_s^T \mathbf{K}^{ss} \Phi_s$ and $[\bar{F}_s] = \Phi_s^T [F_s]$.

2.3. Aeroelastic Modeling. Given the difference of meshing between the aerodynamic and the structure models, an inter-connecting approach must be established between them for aeroelastic analysis, and it can be made using a spline matrix \mathbf{G}_{as} [22]. The transformation from the structural grid node motions $[q_s]$ into the aerodynamic grid node motions $[w]$ can be given by the following:

$$[w] = \mathbf{G}_{as}[q_s]. \quad (31)$$

The transformation formula of the aerodynamic $[F_a]$ and the equivalent value acting on a structural grid $[F_s]$ can be obtained by the following:

$$[F_s] = \mathbf{G}_{as}^T [F_a]. \quad (32)$$

Substituting Equations (31) and (32) into Equation (26), we can obtain the following:

$$[F_s] = \mathbf{Q}[q_s], \quad (33)$$

where \mathbf{Q} is a function of k and rotor rotational velocity Ω and

$$\mathbf{Q}(k, \Omega) = \mathbf{G}_{as}^T [q_d] [\Delta S] [D]^{-1} \mathbf{G}_{as}. \quad (34)$$

Combining Equations (28), (33), and (34), the aeroelastic equation is obtained by

$$\mathbf{M}^{ss}(\Omega, q_s)[\ddot{q}_s] + \mathbf{K}^{ss}(\Omega, q_s)[q_s] = \mathbf{Q}(\Omega, q_s)[\tilde{q}_s] \quad (35)$$

Transforming Eq. (35) to the modal space, the equation can be rewritten as follows:

$$\bar{\mathbf{M}}_s(\Omega, p_s)[\ddot{p}_s] + \bar{\mathbf{K}}_s(\Omega, p_s)[p_s] = \bar{\mathbf{Q}}(k, \Omega)[p_s], \quad (36)$$

where $\bar{\mathbf{Q}}(k, \Omega) = \Phi_s^T \mathbf{Q}(k, \Omega) \Phi_s$.

2.4. Nonlinear Steady-State Solution. The conclusion of the literature [3] shows that the static deformation of the blade will change the structural stiffness, due to the consideration of geometrical nonlinearity, and the aerodynamic force distribution, which will affect the blade flutter stability. Hence, the first step in solving Equation (35) is to get the steady trim

solution in hovering. Dropping the acceleration term, we can write Equation (35) as follows:

$$\mathbf{K}_0^{ss}(\Omega, q_{s0})[q_{s0}] = [F_{s0}], \quad (37)$$

where stiffness matrix \mathbf{K}_0^{ss} is a function of the steady displacement $[q_{s0}]$ and Ω and structural load vector $[F_{s0}]$ is given by the following:

$$[F_{s0}] = \mathbf{G}_{as}^T [q_d] [\Delta S] [D_0]^{-1} [w_0]. \quad (38)$$

The velocity vector $[w_0]$ of Equation (38) is a vector consisting of the normal downwash velocity, which is the normal component of a combined velocity of freestream and induced inflow of the wake, at each panel. For solving the nonlinear aeroelastic equation (37), an iterative algorithm is established in the Isight platform integrating the steady aerodynamic calculation part of self-made MDLM program and the ANSYS software. The process of the algorithm is as follows:

- (1) The initial displacements of the structural grid nodes are set by $[q_{s00}] = 0$. The displacements of the structural grid nodes of the upper wing surface are taken to represent the overall displacement of the blade. The V-g method is used to calculate the blade flutter rotational velocity Ω_F and flutter frequency
- (2) In the i^{th} iteration, where $i = 1, 2, 3, \dots, n$, the displacements of the structural grid nodes are $[q_{s0i-1}]$. The location of structural and aerodynamic grid nodes is refreshed. The normal downwash velocity vector $[w_0]$ and the steady aerodynamic influence coefficient matrix $[D_0]^{-1}$ are recalculated due to the change of the normal direction and the coordinates of sending and receiving points at each panel
- (3) The interpolation matrix \mathbf{G}_{as} is obtained using the Thin Plate Spline (TPS) interpolation method [23]. The steady structural load $[F_{s0}]$ is obtained solving Equation (38)
- (4) The structural grid node displacement vector $[q_{s0i}]$ is calculated using the static structural analysis of ANSYS software when the structural load is applied to the upper wing surface
- (5) If $|[q_{s0i}] - [q_{s0i-1}]| < \varepsilon$, then, the computation converges, and if it does not, then, Steps (2)–(4) are repeated

After the calculation converges, the structure displacement $[q_{s0}]$, the location of structural and aerodynamic grid nodes, and the structural load $[F_{s0}]$ in a static trim state are obtained. Given the large deflection and the geometric nonlinearity, the natural modes of vibration Φ_{s0} , the mass matrix $\mathbf{M}_0^{ss}(\Omega, q_{s0})$, and the stiffness matrix $\mathbf{K}_0^{ss}(\Omega, q_{s0})$ about the equilibrium position are obtained by the prestress modal analysis of ANSYS.

2.5. *Flutter Solution.* The flutter motion $[q_s]$ is assumed to be a small perturbation $[\tilde{q}_s]$ about the equilibrium position $[q_{s0}]$ and can be written as follows:

$$[q_s] = [q_{s0}] + [\tilde{q}_s]. \quad (39)$$

Substituting Equation (39) into Equation (35), we can linearize the flutter equation, based on the assumption of small perturbation, by the following:

$$\mathbf{M}_0^{\text{ss}}(\Omega, q_{s0}) \left[\ddot{\tilde{q}}_s \right] + \mathbf{K}_0^{\text{ss}}(\Omega, q_{s0}) ([\tilde{q}_s] + [q_{s0}]) = \mathbf{Q}(\Omega, q_{s0}) [\tilde{q}_s] + [F_{s0}], \quad (40)$$

Simplified by Equation (37), Equation (40) can be rewritten as follows:

$$\mathbf{M}_0^{\text{ss}}(\Omega, q_{s0}) \left[\ddot{\tilde{q}}_s \right] + \mathbf{K}_0^{\text{ss}}(\Omega, q_{s0}) ([\tilde{q}_s]) = \mathbf{Q}(\Omega, q_{s0}) [\tilde{q}_s]. \quad (41)$$

Transforming Equation (41) into the modal space, the equation can be rewritten as follows:

$$\bar{\mathbf{M}}_{s0}(\Omega, p_{s0}) \left[\ddot{\tilde{p}}_s \right] + \bar{\mathbf{K}}_{s0}(\Omega, p_{s0}) [\tilde{p}_s] = \bar{\mathbf{Q}}(k, \Omega) [\tilde{p}_s], \quad (42)$$

where $\bar{\mathbf{M}}_{s0} = \Phi_{s0}^T \mathbf{M}_0^{\text{ss}} \Phi_{s0}$, $\bar{\mathbf{K}}_{s0} = \Phi_{s0}^T \mathbf{K}_0^{\text{ss}} \Phi_{s0}$, $\bar{\mathbf{Q}}(k, \Omega) = \Phi_{s0}^T \mathbf{Q}(k, \Omega) \Phi_{s0}$, $[\tilde{p}_{s0}] = \Phi_{s0}^T [\tilde{q}_{s0}]$, and $[\tilde{p}_s] = \Phi_{s0}^T [\tilde{q}_s]$.

Based on the assumption of harmonic motion ($[\tilde{p}_s] = [\tilde{p}_{ss}] e^{i\omega t}$) transforming Equation (42) into a frequency domain, the aeroelastic equation can be rewritten as follows:

$$[-\omega^2 \bar{\mathbf{M}}_{s0}(\Omega, p_{s0}) + \bar{\mathbf{K}}_{s0}(\Omega, p_{s0}) - \bar{\mathbf{Q}}(k, \Omega)] [\tilde{p}_s] = 0. \quad (43)$$

Equation (43) is solved in the frequency domain by the V-g method to obtain the flutter rotational velocity of the rotor blade in hovering. A specific process can refer to Ref. 24.

Given the effect of centripetal force, the mass and stiffness matrixes of the blade are the functions of rotational velocity. To match the current rotational velocity to the flutter rotational velocity, we can use an iterative algorithm as follows:

- (1) In the i^{th} iteration, where $i = 1, 2, 3, \dots, n$, for the rotational velocity Ω_i and the collective pitch θ_0 , the static steady-state solution is carried out, and the specific steps can be referred to the abovementioned
- (2) The V-g method is used to calculate the blade flutter rotational velocity Ω_F and flutter frequency f_F
- (3) If $|\Omega_i - \Omega_F| < \epsilon$, the computation converges, and if it does not, $\Omega_{i+1} = \Omega_F$ and Steps (1)–(2) are repeated

TABLE 1: Values of parameters of uniform blade for numerical results.

$k_{m1}/R = 0$	$c/R = \pi/40$	$a = 6$
$k_{m2}/R = 0.025$	$\sigma = 0.1$	$\beta_p = 0.05$
$k_A/k_m = 1.5$	$\gamma = 5$	$C_{D0} = 0.0095$

After the calculation converges, the flutter rotational velocity Ω_F and flutter frequency f_F is obtained for the current blade pitch.

3. Presentation of Results

3.1. *MDLM Validation.* In this work, the steady-state deformation and flutter stability of a hovering rectangular hingeless blade are analyzed. The aeroelastic model is established by combining the moderate deflection beam theory with the MDLM.

The blade is made of isotropic material. Nondimensional natural frequencies in the flap, lead-lag, and torsion directions are $\omega_w = 1.15$, $\omega_v = 1.5$, and $\omega_\phi = 3.0$ or 5.0 , respectively. Table 1 shows other blade nondimensional parameters [3].

Figure 1 exhibits the steady tip deflection w_{tip} , flap and lead-lag bending deflection v_{tip} , and elastic twist angle θ_{tip} with respect to collective pitch θ_0 and the results of Sivaneri and Chopra [3]. The agreement between the two results is good.

Figure 2 shows the flutter stability boundary respect with β_p and the results of Sivaneri and Chopra [3]. The flutter solution is calculated by the V-g method. A general agreement emerges between the two results.

3.2. *Rotational Modal Analysis.* In the present study, the natural frequencies of the swept tip blades were investigated in ANSYS, and the results were compared with those of the experiment [25] to assess the availability of ANSYS for analyzing the dynamic characteristics of rotating hingeless isotropic rotor blades. The blade parameters are the same as those of the beams tested by Epps and Chandra [25]. The radius of the rotor is 1,016 mm, and the hub length is 63.5 mm. In addition, the length of the swept tip segment is 152.5 mm, the width is 25.4 mm, and the thickness is 1.6 mm. The tip sweep angles Λ are 15 and 45 degrees. The isotropic material of the blades is aluminum. The model is 3-D FE model of 2908 nodes and of 360 elements, and the meshing is shown in Figure 3. Figures 4 and 5 show the natural frequencies with respect to the rotating speeds. The results show that the present predictions have a good correlation with the results of the experiment.

3.3. *Flutter Solution.* The flutter rotational velocities of hingeless rotor blades that have swept tips and different aspect ratios are obtained for different collective pitches by the present method mentioned above and the usual

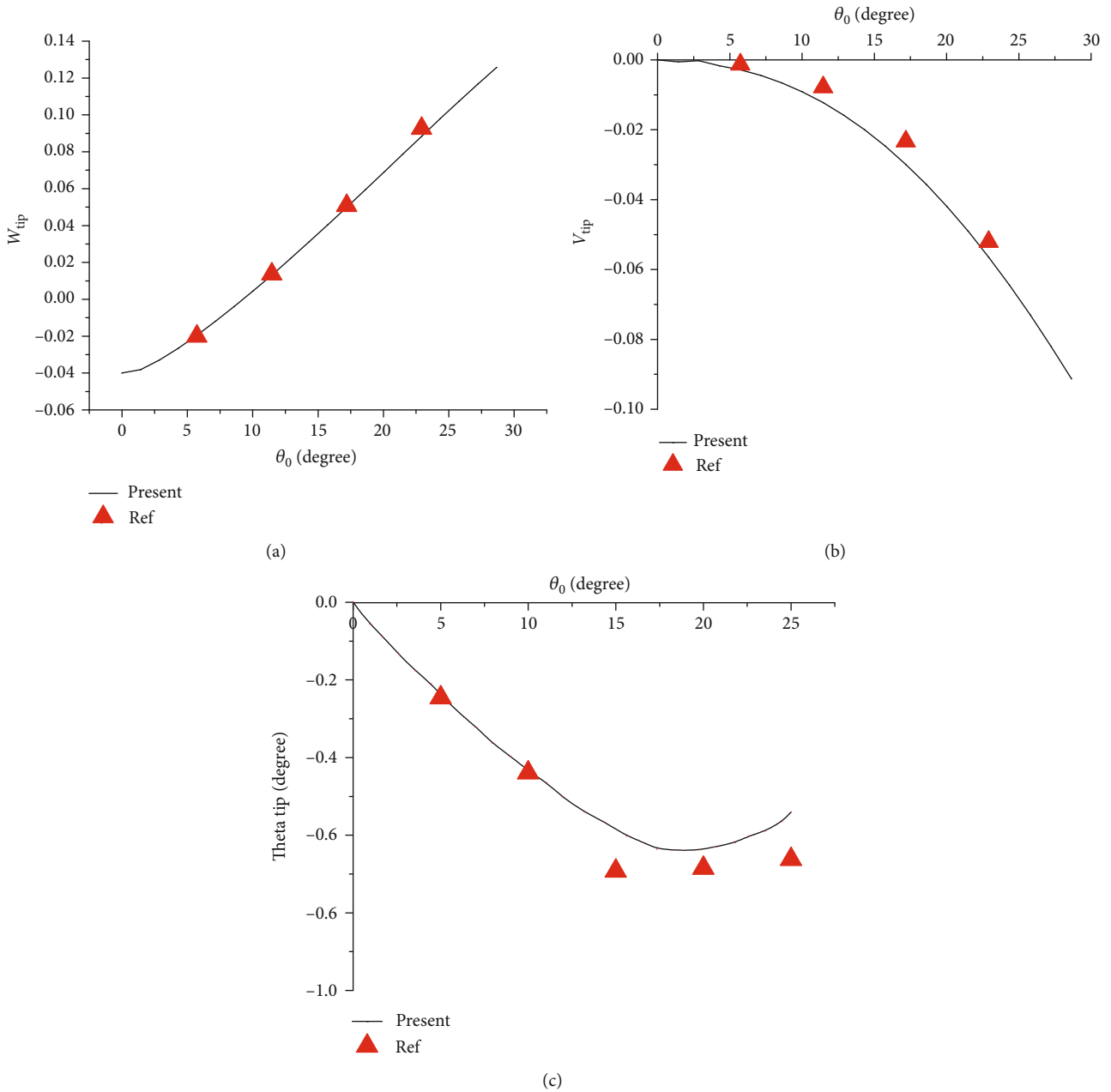


FIGURE 1: Comparison of steady tip deflection by the MDLM and the quasisteady strip theory ($\omega_w = 1.15$, $\omega_v = 1.5$, and $\omega_\phi = 5.0$).

method constructed by unsteady strip aerodynamic theory and large deflection beam theory [4]. The airfoil section of the blade is naca8h12 and is shown in Figure 6. In Figure 6, the elastic axis position is ea , and the distance to the leading edge of the ea is XE . Table 2 shows the parameters of the section. There exists a destabilizing offset, XA , between the aerodynamic center and the elastic axis.

The isotropic material is aluminum. Figure 7 shows the blade platform, which is based on the blade tested by Harder and Desmarais [22] and includes a hub. The radius of the rotor blade is $R = 4.252$ m. Two hub lengths ($h_i = 0.367$ m and 1.5645 m) are considered in investigating the effect of aspect ratios ($AR = 18.07$ and 12.5). The

length of the swept tip segment is $n = 0.6378$ m. The tip sweep angle Λ is 45 degrees.

Table 3 shows natural frequencies of the blade ($AR = 18.07$) at the rotational velocity 400 rpm, as the total number of elements is varied from 4880 to 6710. The results show, for the case considered, that 6100 elements are sufficient for reasonably good convergence.

Figures 8–9 show the flutter rotational velocities, and Figures 10–11 show the V-g diagrams, with respect to various aspect ratios, where $\Omega = 500$ rpm. The results show that the flutter rotational velocities obtained by the present method are evidently lower than those obtained by the usual method. The differences in flutter rotational

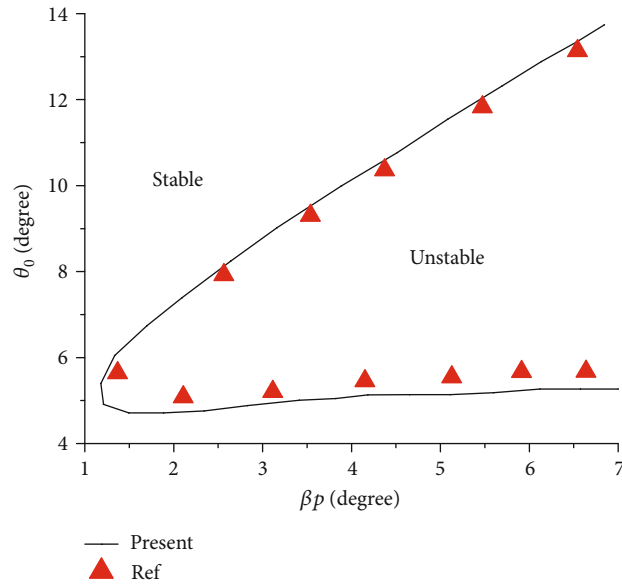


FIGURE 2: Effect of precone on the stability boundaries ($\omega_w = 1.15$, $\omega_v = 1.5$, and $\omega_\phi = 3.0$).

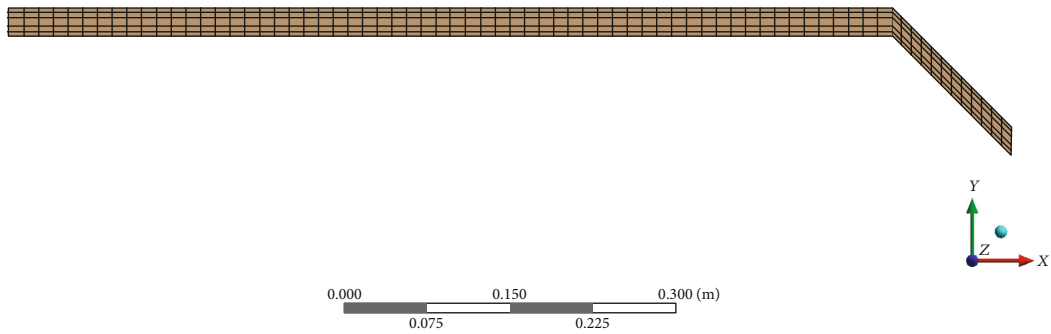


FIGURE 3: Meshing of the blade model.

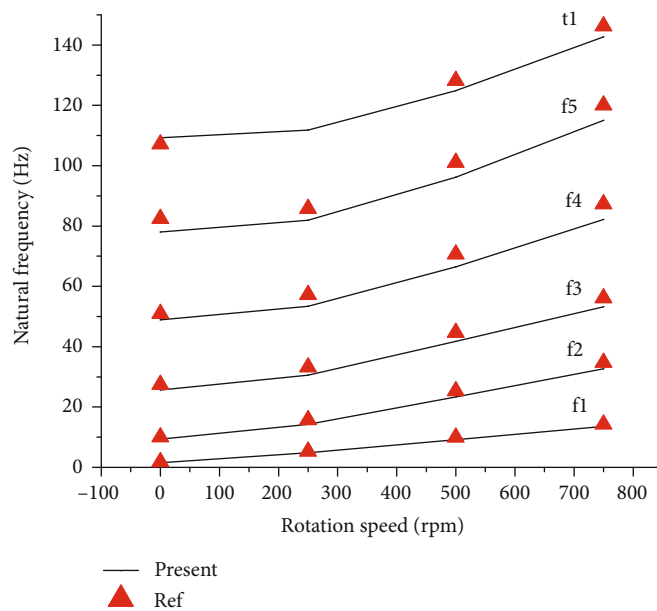


FIGURE 4: Natural frequencies of the blade ($\Lambda = 45^\circ$).

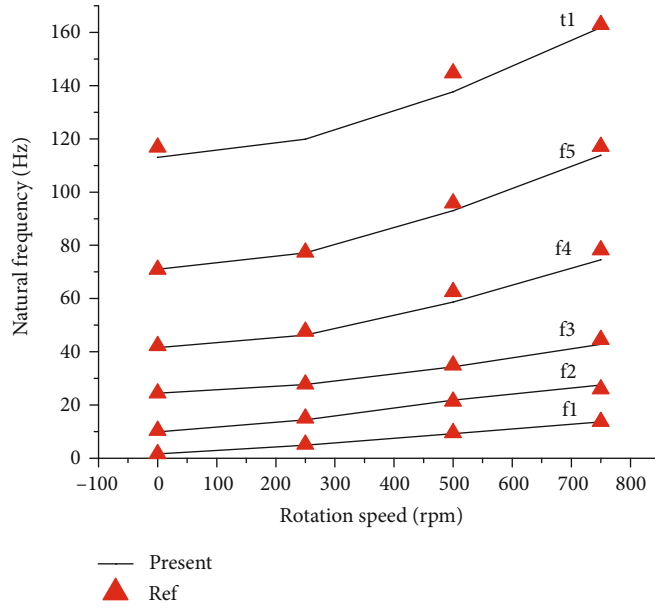


FIGURE 5: Natural frequencies of the blade (Λ = 15°).

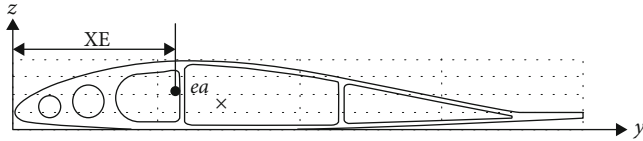


FIGURE 6: Blade section.

TABLE 2: Values of parameters of blade section.

$A = 0.001229 \text{ m}^2$	$I_z = 0.441 \times 10^{-5} \text{ m}^4$	$XA = 0.006704 \text{ m}$
$I_y = 0.766 \times 10^{-7} \text{ m}^4$	$J = 0.244 \times 10^{-6} \text{ m}^4$	$c = 0.215 \text{ m}$
$XE = 0.060454 \text{ m}$		

TABLE 3: Natural frequency of hingeless rotor blade (AR = 18.07).

Number of elements	Mode 1 (Hz)	Mode 2 (Hz)	Mode 3 (Hz)	Mode 4 (Hz)
4880	7.57	11.837	15.508	26.472
5490	7.57	11.837	15.506	26.471
6100	7.5697	11.836	15.505	26.469
6710	7.5696	11.836	15.504	26.467

The cause of the differences may mainly consist of the following two parts:

- (1) The flutter of both conditions occurs between the 2nd mode and the 3rd mode. The modal analysis of these two modes directly affects the flutter result. Figures 12–13 show the frequencies of these modes about steady deflected positions with respect to the rotating speeds ($\theta_0 = 6^\circ$). Figures 14–15 show the shapes of these modes of the blade (AR = 12.5). The 2nd mode is the flap and torsion coupled mode, and the 3rd mode is the lead-lag and torsion coupled mode. The differences in modal analysis between the 1-D beam model and the 3-D finite element model, increasing with the decrease of the aspect ratio, because of strong coupling, generated from geometry, between flap, lag and torsion [12], may cause differences of flutter results

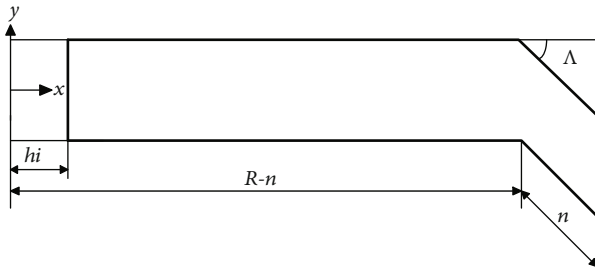


FIGURE 7: Blade planform with tip sweep (Λ = 45°).

velocities between the two methods increase with the decrease of the aspect ratio. When AR = 18.07, the results of the two methods are close, and the differences between the two methods are less than 10%. When AR = 12.5, the differences between them are 10% to 20%.

- (2) In the modal analysis, the blade sections of the 3-D finite element model have deformations, which are not included in the strip theory aerodynamic loadings. But the motions of parts of sections can be

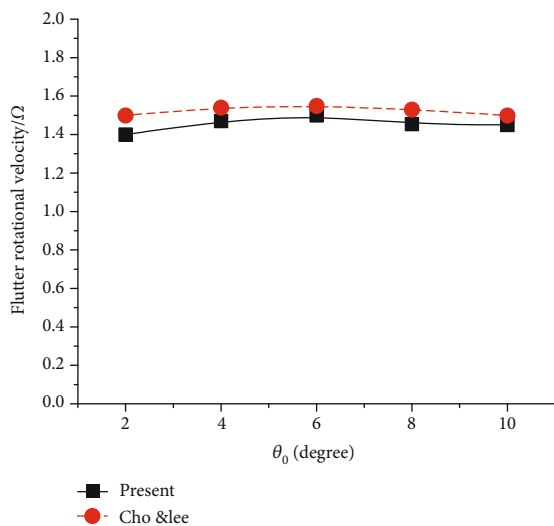


FIGURE 8: Flutter rotational velocities of the blade (AR = 18.07).

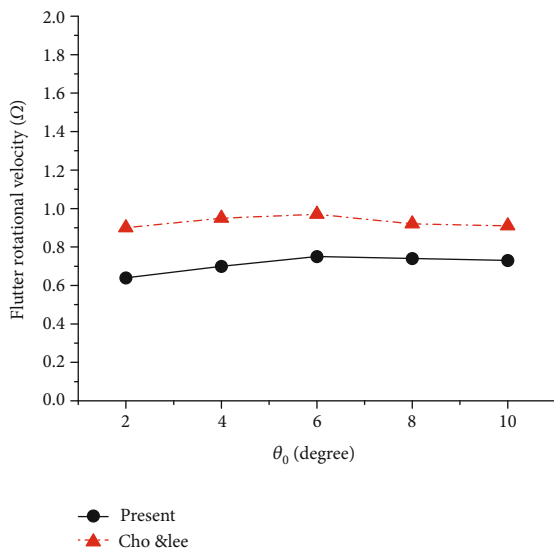


FIGURE 9: Flutter rotational velocities of the blade (AR = 12.5).

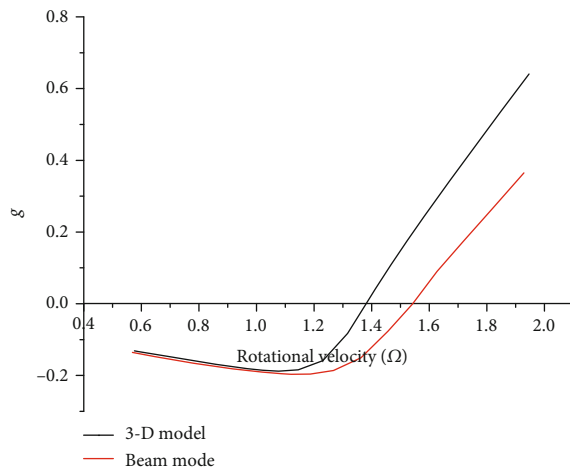


FIGURE 10: V-g diagram of the blade (AR = 18.07).

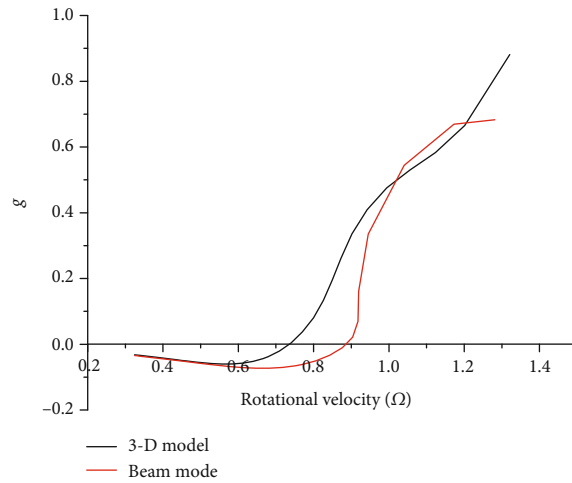


FIGURE 11: V-g diagram of the blade (AR = 12.5).

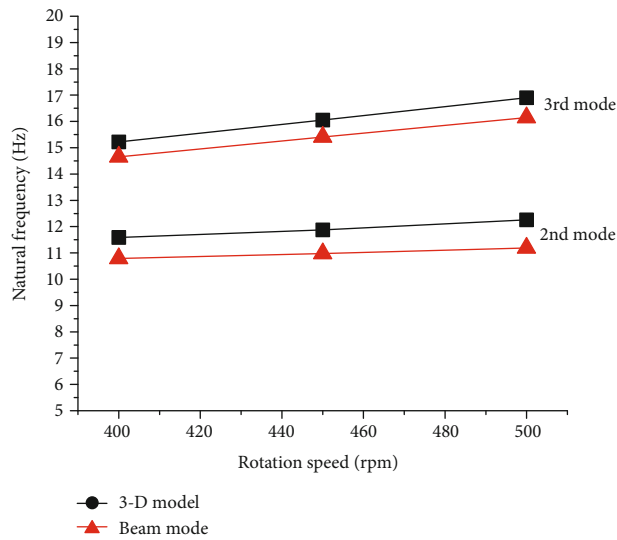


FIGURE 12: Natural frequencies (AR = 18.07).

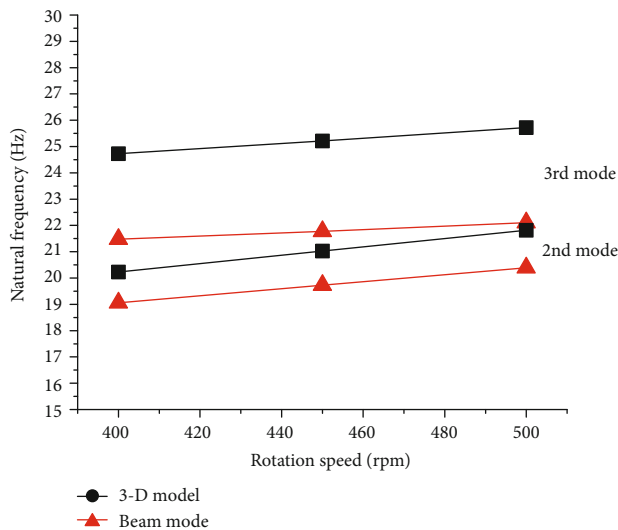


FIGURE 13: Natural frequencies (AR = 12.5).

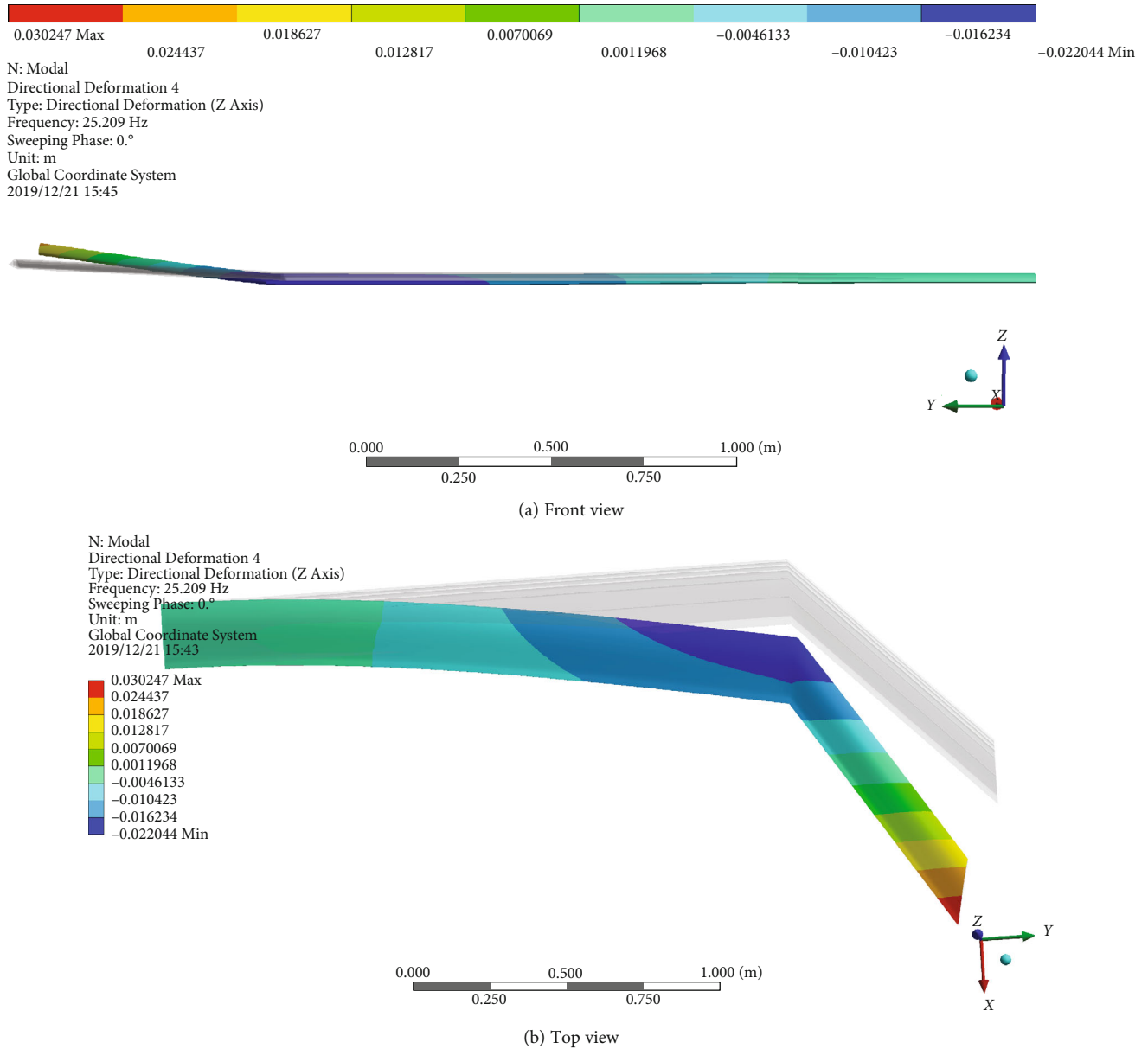


FIGURE 14: Lead-lag/torsion coupled mode.

considered in the MDLM. Figures 16–17 show the displacements of the 3-D finite element nodes at $r = 0.75R$ in the Flap/torsion coupled mode about the steady deflected positions. The results show that the deformations of sections increase with the decrease of aspect ratio

4. Conclusion

- (1) The results of steady-state deflection and the flutter stability boundaries show that the MDLM is reliable in the steady and unsteady aerodynamic calculations
- (2) The dynamic characteristics of rotating blades obtained by the modal analysis of ANSYS show good agreement with the experiment

- (3) The flutter solutions of the blades with advanced geometric configurations are obtained by the new method, based on the MDLM and ANSYS-based structural analysis, and the usual method, based on strip theory and the beam theory model. The flutter rotational velocities obtained by the present method are lower than those obtained by the usual method. The differences of flutter rotational velocities between the two methods increase with the decrease of the aspect ratio. The distinctions may arise mainly from the differences of modal analysis between the 1-D beam model and the 3-D finite element model and the warping of the blade sections. Hence, the method of this paper is more suitable for the flutter stability analysis of advanced geometric blades than the usual method

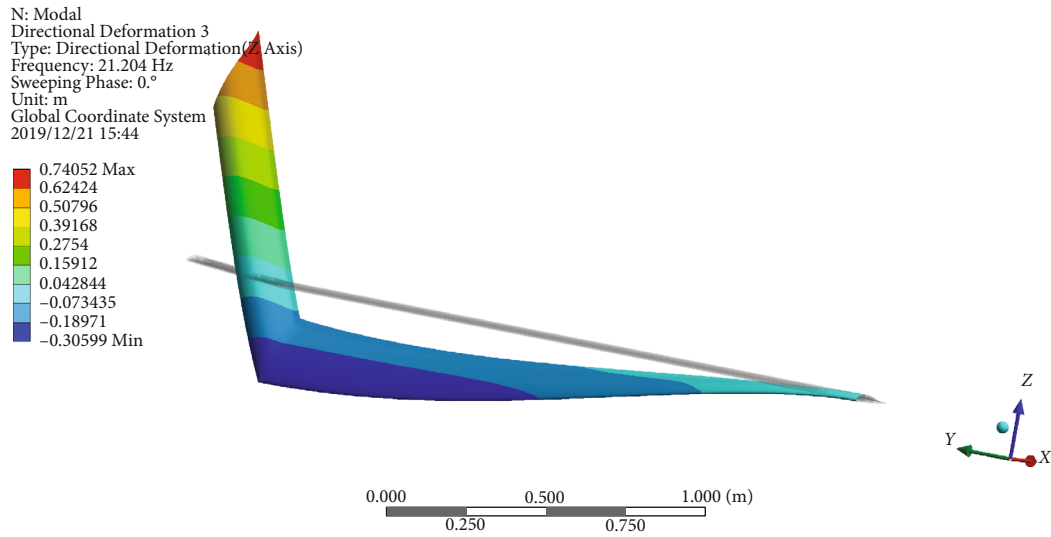


FIGURE 15: Flap/torsion coupled mode.

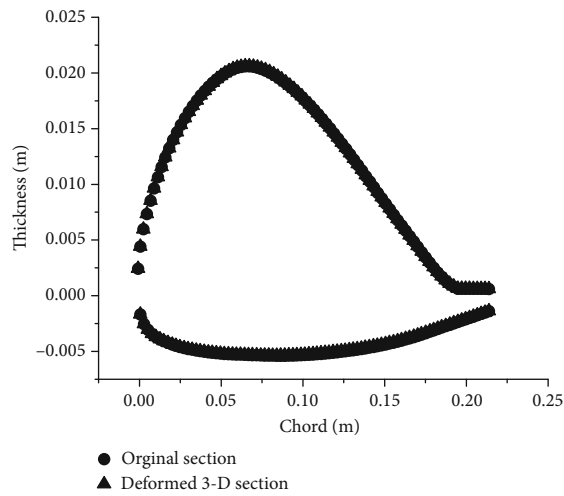


FIGURE 16: Deformed sections of 3-D model (AR = 18.07).

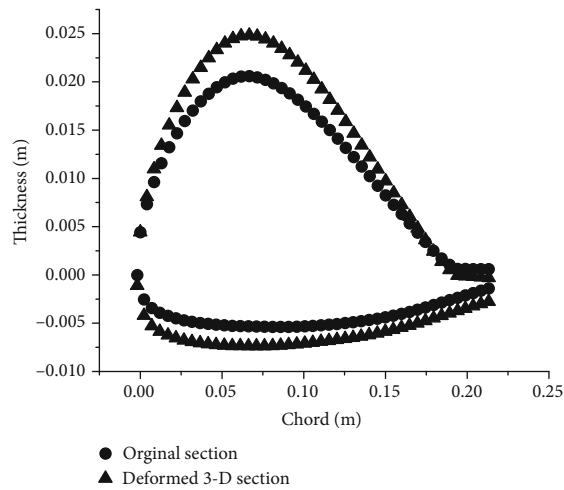


FIGURE 17: Deformed section of 3-D model (AR = 12.5).

Nomenclature

$\Delta\bar{p}$:	Pressure loading
q_d :	Velocity pressure number
ω :	Circular frequency of vibration
Ψ_s, Ψ_d :	Anhedral of the receiving point and sending point
S_j :	Area of the j th panel
$\Delta\bar{p}$:	Pressure difference on the unit length of 1/4 chord of the j th panel
D_{0ij} :	Steady downwash factor
$[c_p]$:	Differential pressure coefficient vector
\mathbf{M}^{ss} :	Structural mass matrix
$[q_s]$:	Displacement vector
Ω :	Rotor blade rotational velocity
\mathbf{G}_{as} :	Spline matrix
\mathbf{M}_s :	Structural mass matrix in modal space
\mathbf{K}_0^{ss} :	Structural stiffness matrix at trim position
$[F_{s0}]$:	Steady structural load vector
$\omega_v, \omega_w, \omega_\phi$:	Fundamental coupled rotating lead-lag, flap, and torsion natural frequencies, respectively
k_m :	Mass radius of gyration of blade cross section ($k_m = \sqrt{k_{m1}^2 + k_{m2}^2}$)
σ :	Solidity ratio
a :	Lift curve slope
C_{D0} :	Blade section profile drag coefficient
ea :	Elastic axis position
I_y, I_z, J :	Cross-section moments of inertia in the flap, lead-lag, and torsion directions, respectively
U_∞ :	Free-flow velocity
M_∞ :	Free-flow Mach number
n_c, n_d :	Normal vector of the receiving point and the sending point
U_j :	Freestream velocity of the j th panel
$\Delta\bar{p}_j$:	Pressure difference per unit area of the j th panel
$\Delta\bar{c}_{pj}$:	Coefficient of pressure difference
D_{1ij}, D_{2ij} :	Incremental oscillatory downwash factors
$[F_a]$:	Aerodynamic load vector
\mathbf{K}^{ss} :	Structural stiffness matrix
$[F_s]$:	Structural load vector
Φ_s :	Modal matrix
$[P_s]$:	Displacement vector in modal space
\mathbf{K}_s :	Structural stiffness matrix in modal space
$[q_{s0}]$:	Blade steady displacement
$[w_0]$:	Steady normal downwash velocity vector
k_{m1}, k_{m2} :	Principal mass radii of gyration of blade cross-section
k_A :	Polar radius of gyration of blade cross section
γ :	Lock number
β_p :	Blade precone angle
XE:	Distance to the leading edge of ea
XA:	Destabilizing offset between aerodynamic center and elastic axis.
A:	Area of the blade section.

Data Availability

The data used to support the findings of this study are available from the corresponding author upon request.

Conflicts of Interest

The authors declare that they have no conflicts of interest.

Acknowledgments

This study was cosupported by the National Natural Science Foundation of China (No. 11472133) and a project funded by the Priority Academic Program Development of Jiangsu Higher Education Institutions.

References

- [1] P. Friedmann, "Aeroelastic instabilities of hingeless helicopter blades," *Journal of Aircraft*, vol. 10, no. 10, pp. 623–631, 1973.
- [2] P. Friedmann and C. Yuan, "Effect of modified aerodynamic strip theories on rotor blade aeroelastic stability," *AIAA Journal*, vol. 15, no. 7, pp. 932–940, 1977.
- [3] N. T. Sivaneri and I. Chopra, "Dynamic stability of a rotor blade using finite element analysis," *AIAA Journal*, vol. 20, no. 5, pp. 716–723, 1982.
- [4] M. H. Cho and I. Lee, "Aeroelastic stability of hingeless rotor blade in hover using large deflection theory," *AIAA Journal*, vol. 32, no. 7, pp. 1472–1477, 1994.
- [5] D. H. Hodges, "Geometrically exact, intrinsic theory for dynamics of curved and twisted anisotropic beams," *AIAA Journal*, vol. 41, no. 6, pp. 1131–1137, 2003.
- [6] M. R. Amoozgar, H. Shahverdi, and A. S. Nobari, "Aeroelastic stability of hingeless rotor blades in hover using fully intrinsic equations," *AIAA Journal*, vol. 55, no. 7, pp. 2450–2460, 2017.
- [7] M. V. Fulton and D. H. Hodges, "Aeroelastic stability of composite hingeless rotor blades in hover—Part II: Results," *Mathematical and Computer Modelling*, vol. 18, no. 3–4, pp. 19–35, 1993.
- [8] P. P. Friedmann, K.-A. Yuan, and M. de Terlizzi, "An aeroelastic model for composite rotor blades with straight and swept tips. Part I: Aeroelastic stability in hover," *International Journal of Non-Linear Mechanics*, vol. 37, no. 4–5, pp. 967–986, 2002.
- [9] H. Yeo, M. Potsdam, and R. A. Ormiston, "Application of CFD/CSD to rotor aeroelastic stability in forward flight," in *66th American Helicopter Society Annual Forum Proceedings*, Phoenix, Arizona, May 2010.
- [10] J. Han, Q. Chen, and H. Yun, "Aeroelasticity of helicopters," *Acta Aeronautica et Astronautica Sinica*, vol. 36, no. 4, pp. 1034–1055, 2015.
- [11] W. Zhang, B. Wang, and Z. Ye, "High efficient numerical method for limit cycle flutter analysis based on nonlinear aerodynamic reduced order model reduced order model," in *51st AIAA/ASME/ASCE/AHS/ASC Structures, Structural Dynamics, and Materials Conference*, Orlando, Florida, New York, April 2010.
- [12] B. G. van der Wall, C. Kessler, Y. Delrieux et al., "From aeroacoustics basic research to a modern low-noise rotor blade," *Journal of the American Helicopter Society*, vol. 62, no. 4, pp. 1–16, 2017.
- [13] K. V. Truong, *Dynamics studies of the ERATO blade, based on finite element analysis*, vol. 2005, 31st European Rotorcraft Forum, Florence, Italy, 2005.

- [14] H. Yeo, K. V. Truong, and R. A. Ormiston, "Comparison of one-dimensional and three-dimensional structural dynamics modeling of advanced geometry blades," *Journal of Aircraft*, vol. 51, no. 1, pp. 226–235, 2014.
- [15] Y. J. Kee and S. J. Shin, "Structural dynamic modeling for rotating blades using three dimensional finite elements," *Journal of Mechanical Science and Technology*, vol. 29, no. 4, pp. 1607–1618, 2015.
- [16] A. B. Guimarães Neto, R. G. A. da Silva, and P. Paglione, "Control-point-placement method for the aerodynamic correction of the vortex- and the doublet-lattice methods," *Aerospace Science and Technology*, vol. 37, pp. 117–129, 2014.
- [17] M. Brendel and E. Sulaeman, "Improved doublet lattice formulation for calculating aerodynamic loads on lifting surfaces in unsteady subsonic flow," in *12th Applied Aerodynamics Conference*, Colorado Springs, USA. New York, 1994.
- [18] M. T. Landahl, "Kernel function for nonplanar oscillating surfaces in a subsonic flow," *AIAA Journal*, vol. 5, no. 5, pp. 1045–1046, 1967.
- [19] T. P. Kalman, W. P. Rodden, and J. P. Giesing, "Application of the doublet-lattice method to nonplanar configurations in subsonic flow," *Journal of Aircraft*, vol. 8, no. 6, pp. 406–413, 1971.
- [20] S. G. Hedman, "Vortex lattice method for calculation of quasi-steady state loadings on thin elastic wings," Tech. Rep. 105, Aeronautical Research Institute of Sweden, Stockholm, Sweden, 1967.
- [21] D. H. Hodges and R. A. Ormiston, "Stability of elastic bending and torsion of uniform cantilevered rotor blades in hover," in *14th Structures, Structural Dynamics, & Materials Conference*, Williamsburg, New York, USA, March 1973.
- [22] R. L. Harder and R. N. Desmarais, "Interpolation using surface splines," *Journal of Aircraft*, vol. 9, no. 2, pp. 189–191, 1972.
- [23] R. Franke, "Thin plate splines with tension," *Computer-Aided Geometric Design*, vol. 2, no. 1-3, pp. 87–95, 1985.
- [24] P. C. Chen, "Damping perturbation method for flutter solution: the g-method," *AIAA Journal*, vol. 38, no. 9, pp. 1519–1524, 2000.
- [25] J. J. Epps and R. Chandra, "Experimental-theoretical study of the effects of tip sweep on the natural frequencies of rotating composite beams," in *35th AIAA Structures, Structural Dynamics and Materials Conference*, Hilton Head, South Carolina. New York, April 1994.